Effect of Temperature, Time, and Cooling Rate on the Mineralogy, Morphology, and Reducibility of Iron Ore Sinter Analogues

TOBIN HARVEY [ORCID],[1] MARK I. POWNCEBY,[2] JEFF CHEN,[3] NATHAN A.S. WEBSTER,[2] THI BANG TUYEN NGUYEN,[1] LEANNE MATTHEWS,[1] DAMIEN O'DEA,[4] and TOM HONEYANDS[1,5]

1.—The Australian Research Council (ARC) Research Hub for Advanced Technologies for Australian Iron Ores, University of Newcastle, Callaghan, NSW 2308, Australia. 2.—CSIRO Mineral Resources, Clayton, VIC 3168, Australia. 3.—Centre for Advanced Microscopy, Australian National University, Canberra, Australia. 4.—Marketing Iron Ore, BHP, Brisbane, QLD 4000, Australia. 5.—e-mail: tom.a.honeyands@newcastle.edu.au

Analogue sinter tablets were produced at temperatures between 1250°C and 1320°C, with a range of hold times and cooling rates. Platy silico-ferrite of calcium and aluminum (SFCA) morphology was identified in samples produced at 1250°C using reflected light microscopy; however, quantitative x-ray diffraction (XRD) identified the presence of the SFCA phase, with no SFCA-I detected. This proves that the platy SFCA morphology common in analysis by reflected light microscopy cannot be attributed to the SFCA-I mineral without further analysis. Micro-XRD and electron probe micro-analysis (EPMA) were carried out on an area of platy SFCA confirming this result. The sinter analogue tablets were reduced in a 30% CO, 70% N_2 gas mixture at 900°C in a tube furnace thermo-gravimetric analyzer. The degree of reduction of the tablets in this study was found to be controlled by the porosity of the samples, rather than by the morphology or mineralogy of the bonding phase.

INTRODUCTION

The continued growth of iron and steelmaking, combined with environmental pressure to reduce greenhouse gas emissions, makes the optimization of the iron ore sintering process more important than ever. Sintering is a process by which a mixture of fine-grained iron ores (< 6.3 mm), fluxes, and coke are agglomerated in a sinter plant to manufacture a sinter product of a suitable composition, quality, and granulometry to be used as burden material in the blast furnace. Key quality parameters important for producing a good sinter include high strength, low impurities, high porosity and permeability, and high reducibility. All of these are influenced in some way by the mineralogy of the sinter, which in turn is dependent on variables such as temperature, composition, and fuel.

In an attempt to understand and improve the properties of sinter, many authors have studied the mineralogy and morphology of iron ore sinter, with a focus on the bonding phase that is formed as a result of the high-temperature reactions. In order to generate a suitable sinter for ironmaking, the bonding phase must be physically strong, permeable to reducing gases in the blast furnace and easily reduced. Over the past 50 years, a significant body of work has demonstrated that the bonding phase that develops in fluxed iron ore sinters is composed of a complex solid solution phase related to calcium ferrites, but given the general acronym SFCA (silico-ferrite of calcium and aluminum).[1,2]

Beginning with work by Sasaki and Hida (1982)[3] and confirmed more recently by Scarlett et al. (2004)[4] and Webster et al. (2012),[5] it was recognized that SFCA-I and SFCA are stable in discrete compositional and thermal ranges, each having a discrete crystallographic structure. SFCA-I forms at lower temperatures, typically in the range 1180–

1250°C, while SFCA is formed at higher temperatures > 1250–1300°C and may also crystallize from a melt upon cooling.[5,6] SFCA-I is high in iron and low in silica, with approximate composition of 84 wt% Fe_2O[3,7] wt% CaO, 1 wt% SiO_2, and 2 wt% Al_2O_3[11]; SCFA is low in iron and high in silica, with approximate composition of 60–76 wt% Fe_2O[3,7–10] wt% CaO, 3–10 wt% SiO_2[4–6,11–14] wt% Al_2O_3, and 0.7–1.5 wt% MgO.[1,2,12] Recently Mumme (2003)[13] and Webster et al. (2012)[5] have identified additional forms of SFCA, denoted as SFCA-II and Fe-rich SFCA, respectively. The importance of these phases in industrially produced iron ore sinter is thought to be negligible.

Early work which pointed to the importance of SFCA phases for sinter quality came from dissection of blast furnaces in the 1980s.[14] Examination of samples from the shaft of the blast furnace revealed that platy SFCA ("acicular calcium ferrite"), identified via texture using reflected light microscopy, was more reduced than prismatic SFCA ("columnar calcium ferrite"). The use of similar definitions of SFCA based on morphology using reflected light microscopy or scanning electron microscopy has become common in industry and academia, with a good review provided by Nicol et al. (2018).[15] Furthermore, it is common to assume that the platy and columnar morphologies correspond to the SCFA-I and SFCA minerals, respectively. As pointed out by Nicol et al.,[15] however, the use of morphological features to identify and distinguish between SFCA and SFCA-I minerals has resulted in the generation of a number of conflicting textural terms used for the same phase. It is likely that many of the diverse textural features result from differences in sintering conditions of temperature and cooling rates, with the possibility of one or both 'SFCA' phases generating a similar, if not the same, texture. The authors' previous work examined the properties of several industrial and pilot-scale sinters using a range of techniques, and concluded that the alignment of morphological and x-ray diffraction (XRD) definitions was not possible.[16] Other work by Mezibricky and Frolichova[7] and Takayama et al.[8] has demonstrated that using a morphological approach to distinguishing between SFCA and SFCA-I types is problematic, since both phases can exhibit similar textures. Similarly, Cai et al.[9] produced both columnar and acicular (i.e., platy) textures of SFCA in their work, identifying both as SFCA using XRD.

More recent work has focused on the reducibility of sinter and sinter phases, and several authors have been able to link mineralogy to reducibility, concluding that SFCA-I, identified by XRD, is more reducible than SFCA.[10] Cai et al.[9] and Murakami et al.[17] examined the reducibility of samples based on texture, rather than mineralogy, concluding that the acicular form of SFCA (i.e., platy) was more reducible. Similarities in chemistry of the SFCA group of phases together with overlapping morphologies means that current characterization techniques, often used in isolation, allow either the microstructures or the proportion of mineral phases present to be determined, but not the mineral phases present in particular microstructures. This information would inform the design of analysis systems to allow the quality of industrial sinters to be measured.

The aim of this paper is to use analogue sinter tablets, representing matrix bonding phase compositions, to examine the effect of temperature, time, and cooling rate on phase formation in iron ore sinter. A combination of techniques are used to examine the morphology (reflected light optical microscopy), determine the mineralogy (XRD and micro-XRD) and the chemistry (electron probe microanalysis; EPMA). The reducibility of the analogue sinter tablets was also measured, and the relationship between mineralogy, texture, and reducibility is discussed.

EXPERIMENTAL

Sinter Analogues

Sinter analogues designed to simulate the bonding phase in iron ore sinter were prepared from Australian iron ore fines using an infra-red rapid-heating furnace. The equipment and procedure is described in previous work.[18] A 1-mm fraction of the iron ore was fluxed to a binary basicity (CaO/SiO_2 ratio) of 2.0 using reagent grade $CaCO_3$ with SiO_2 of 5.4%, MgO of 1.8%, Al_2O_3 of 2.5%, and the remainder being Fe_2O_3. The analogue tablets were heated following the temperature profile given in Fig. 1, which is based on temperature measurements from sinter pot tests.[19] The rapid-heating furnace allowed independent control of the maximum temperature, hold time, and cooling rate for each experiment. The conditions used in these experiments are shown in Table I. The enclosed area (EA) is the integration of the time (min) spent at a temperature above 1100°C, and is often used as a measure of the energy input to the sintering process. Bottled gas with 0.5% O_2 in N_2 ($pO_2 = 5 \times 10^{-3}$ atm) was injected into the furnace at 0.5 L/
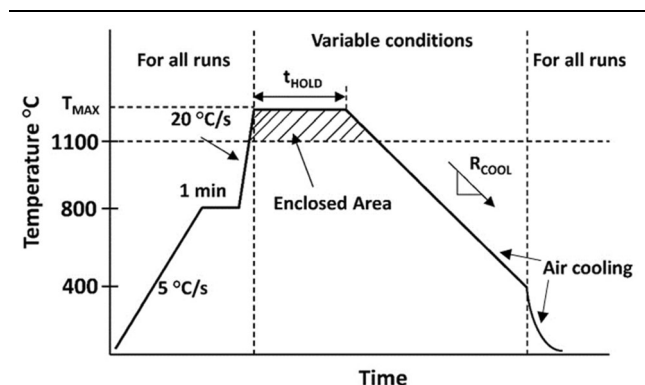

Fig. 1. Set point temperature profile in the rapid heating furnace.

Table I. Analogue sinter tablet experimental conditions

Sample #	Maximum temperature (°C)	Holding time (min)	Cooling rate (°C/s)	Enclosed area 1100°C (°C/min)
1	1250	1	5	197
2	1250	1	1	347
3	1250	4	5	647
4	1250	4	1	797
5	1285	0.17	5	102
6	1285	1	5	256
7	1285	2.5	3	572
8	1285	4	1	1039
9	1320	0.17	5	138
10	1320	1	5	321
11	1320	1	1	644
12	1320	4	5	981
13	1320	4	1	1304

min during heating and for the hold time at the maximum temperature.[20] During cooling, the gas was switched to air at the same flow rate.

Reflected Light Microscopy

Analogue sinters were crushed and mounted in epoxy resin before being cut and ground to expose the viewing surface. Sample blocks were then polished to a mirror finish and viewed using a Zeiss Axioscope optical microscope with an automatic stepping stage. Quantitative textural data were collected using point counting following the mineral classification scheme detailed in Honeyands.[16]

X-ray Diffraction

Approximately 0.6 g of the sinter pellet was micronized in a McCrone micronizing mill (Westmont, IL, USA) under ethanol to reduce the particle size for quantitative XRD (QXRD) analysis ($\approx 10~\mu$m). Diffraction data were collected from 5 to 140° 2θ using a Panalytical MPD instrument (Almelo, The Netherlands) fitted with a cobalt long-fine-focus X-ray tube operating at 40 kV and 40 mA. The incident beam path was defined using 0.04 rad Soller slits, a 20-mm mask, a 0.5° fixed divergence slit and a 1° anti-scatter slit. The diffracted beam incorporated a second set of Soller slits, a graphite monochromator to eliminate unwanted wavelengths, and a 4.6-mm anti-scatter slit. An X'Celerator detector was used in scanning line (1D) mode with an active length of 2.122° 2θ and a step size of 0.0167° 2θ. Crystalline phase identification was carried out using an X'Pert HighScore Plus (Malvern Panalytical, 2014).[21] Quantitative phase analysis was achieved using the Rietveld method[22] with the software TOPAS V5 (Bruker AXS, 2013).[23]

Electron Probe Microanalysis

EMPA analyses were obtained using a JEOL Superprobe electron microprobe analyzer (Model JXA 8500F) equipped with five wavelength dispersive spectrometers (WDS) and two Bruker XFLASH 5010 silicon drift detector energy dispersive spectrometers (SDD-EDS). Samples were analyzed using automated EPMA mapping to generate mineral phase maps to illustrate textural features and the distribution of phases. Chemical information for individual phases was obtained by combining the EDS X-ray data obtained at each map pixel to give a chemical phase composition. In addition, WDS-based X-ray quantification was obtained for the SFCA phases, hematite and magnetite. Procedures for each of the techniques used are provided below.

For characterization by EPMA mapping, the polished grain mounts were mapped over a grid of analysis points using a combination of wavelength dispersive (WD) and energy dispersive (ED) spectroscopic techniques. The elements mapped using the WD spectroscopic techniques were Al, Si, Ca, Fe, and Mg. Elements that were not measured by WD spectroscopy were measured using two ED spectrometers operating in parallel. Measuring both ED and WD signals simultaneously ensured that the complete chemical spectrum, at each step interval in the map, was obtained.

Operating conditions for the microprobe during mapping were an accelerating voltage of 12 keV, beam current of 50 nA, step size of 0.5 μm (in x and y), and a counting time of 30 ms per step. Following mapping, the element distribution data obtained were manipulated using the software package CHIMAGE[24] which incorporates an automated clustering algorithm that identifies chemically alike phases.[25] The clustering procedure used was a multi-element data analysis approach, whereby the groupings of elements identified via the clustering algorithm represented statistically different chemical/mineral phases. These phases were then overlaid onto the mapped region to provide a "phase-patched" map showing the distribution of all or selected chemical/mineral phases within the mapped area.

Quantitative WDS analyses were also obtained on the SFCA phases plus hematite and magnetite. For the quantitative analyses, the microprobe was operated at 15 kV and 30 nA and the electron beam defocused to 2 μm (to account for any within-grain inhomogeneity). Counting times were 20 s. on the main peak and 10 s on the background. The suite of elements analyzed included Al, Si, Mn, Fe, P, Mg, and Ca. Oxygen was calculated by stoichiometry, based on valence of the cations assigned. Elemental analyses were corrected for atomic number (Z), absorption (A) and fluorescence (F) using the PAP procedure of Pouchou and Pichoir.[26,27]

Micro X-ray Diffraction

Micro X-ray diffraction analysis was carried out on a selected area of sample 2 with a Malvern Panalytical Empyrean Series 3 using CoKa radiation. The instrument was equipped with a polycapillary focusing X-ray lens (beam diameter 50 ± 5 μm at sample position), an Fe Kb filter, a motorized -stage with automatic z-adjustment and a PIXcel3D detector (1D scanning mode, 3.347° active length). The samples were analyzed over the range 7–60° 2θ, with a step width of 0.0,262,606° 2θ and a total dwell time of 3122 s/step. Phase identification was carried out with the software DiffracPlus Eva 10[28] and the ICDD PDF-2 database.[29]

Reducibility

The reducibility of whole analogue sinter tablets was measured using a tube furnace thermogravimetric analyzer (TGA) utilizing an analytical balance with precision of ± 0.1 mg. The conditions for the test were based on the ISO standard reducibility test for iron ores[30] (ISO7215, 2015), comprising a gas atmosphere of 30% CO and 70% nitrogen, and an isothermal reduction at 900°C for up to 90 min.

The porosity of the analogue sinter tablets was measured using mercury intrusion porosimetry (Micrometrics® AutoPore IV).

RESULTS

Mineralogy and Morphology of Sinter Analogues

The results of the point counting are given in Table II for each of the experimental conditions. The primary hematite content of the analogues generally decreases with increasing maximum temperature and hold time, as more assimilation of the iron ore particles occurs into the calcium ferrite melt.[31] Primary hematite is replaced with secondary hematite and SFCA at a temperature of 1285°C, and with secondary hematite, SFCA (columnar) and magnetite at 1320°C.

The morphology of SFCA is a mixture of platy and columnar at 1250°C, and 1285°C with short holding times at the maximum temperature. As the holding times and maximum temperatures are increased, the morphology becomes dominated by columnar SFCA. These results are aligned with the temperature stability ranges for SFCA-I and SFCA,[5] which tempts the researcher to assume that the platy SFCA morphology is identical to the SFCA-I mineral.

A comparison of duplicate samples with the same maximum temperature and holding time, but slower cooling rate (e.g., samples 12 and 13), suggests that re-oxidation of magnetite to secondary hematite occurs during cooling in air. This is consistent with the previous work of Hsieh and Whiteman (1989).[20]

A selection of sinter analogue samples with a range of SFCA morphologies were selected for analysis using bulk XRD. The results of the bulk XRD examination are shown in Fig. 2. A comparison of the morphology results from point counting and bulk XRD is given in Table III, with the volume % measured in point counting converted to mass% using the densities reported in Honeyands et al. (2019).[16] The XRD results indicate that, for all the samples, the main phases present were hematite, magnetite, SFCA, and dicalcium silicate. Note that, since XRD is a mineralogical characterization method, differences in morphology between phases such as primary and secondary hematite are not determined. Hence, when comparing hematite results from the bulk XRD dataset with the optical data, the primary and secondary hematite abundances have been combined. In general, agreement between phases such as magnetite and larnite is very good, with the exception being a higher SFCA and lower total hematite content measured by XRD compared to the point count data. It can be seen that, while point counting has measured 18.8–21.6% platy SFCA in the sinter analogues 1 and 2, respectively, no SFCA-I was identified in these samples examined using bulk XRD. This strongly indicates that a platy morphology is not diagnostic for the presence of SFCA-I.

The lack of SFCA-I in sample 2 was confirmed by in situ micro-XRD which was applied to areas of platy SFCA identified by point counting. Micro-X-ray diffraction brings XRD analysis to the microscopic scale, allowing correlation of crystal structural information to other microscopic data (e.g., data from the optical microscope) and microanalytical data (e.g., chemical data from EPMA) on an area-by-area basis. As can be seen from Fig. 3, based on the texture/morphology of the platy SFCA present in the selected area, it could be erroneously identified as SFCA-I by conventional point counting method using reflected light microscopy. Results from micro-XRD, however, unambiguously indicate the area analyzed consists of only SFCA and hematite phase.

The results of the comparison between mineralogy determined by reflected light microscopy versus that determined by XRD demonstrate that a platy SFCA morphology cannot be assumed to indicate

Table II. Analogue sinter tablet morphology determined by point counting (volume %)

Sample #	1° Hem[a]	2° Hem[b]	Magnetite	Platy SFCA	Columnar SFCA	C2S[c]	Glass	Quartz	Other[c]
1	48.4	3.1	4.6	18.8	17.9	2.2	1	1.8	2.2
2	41.9	2.4	1.6	21.6	27.5	1.8	0.4	2.2	0.6
3	42	14.9	3	12.1	23.1	0.4	2	1.6	0.9
4	32.7	13.9	1.4	4.3	44.3	0	2.4	0.4	0.6
5	56.5	0.4	0.4	33.1	4.1	0	1	3.9	0.6
6	44.6	11.2	3.7	20.5	17.9	0	0.6	0.2	1.3
7	18	29	3.6	5.5	38.5	2.1	1.7	0.2	1.4
8	15.2	34.4	2.6	2	41.5	1.7	2.4	0.2	0
9	50.6	2.2	1	29.8	12	0	2	1.8	0.6
10	17.5	23.2	17.3	2.2	29.1	6.1	4.3	0.2	0.1
11	14.2	26.7	11.7	1.4	41.5	1.7	2.3	0	0.5
12	1	13.4	45.7	0.4	25.7	5.2	8.1	0	0.5
13	3.4	26.9	31.3	0	32.6	2.1	3.6	0	0.1

[a]1° Hem indicates primary, unreacted hematite[b]2° Hem indicates secondary hematite[c]C2S refers to 2CaO.SiO$_2$[d]Other refers to unreacted fluxes.
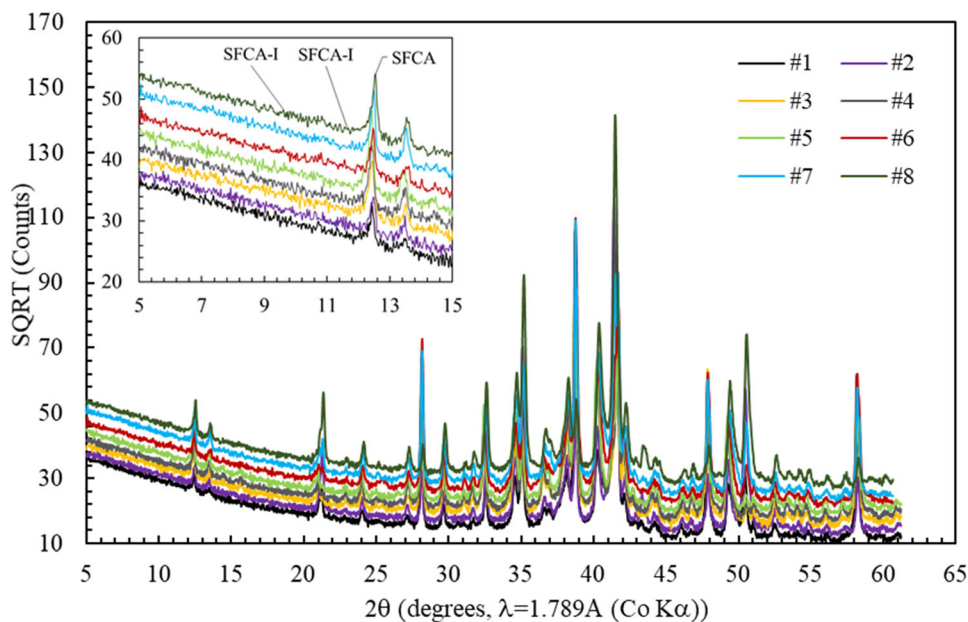

Fig. 2. Bulk XRD patterns for selected, representative sinter analogue samples.

the presence of SFCA-I phase. While SFCA-I has been shown to be stable at lower temperatures (Webster et al., 2012), the conditions that samples 1 and 2 were run at are likely to be above the stability of SFCA-I. The results presented here indicate that the low-temperature form of SFCA can also exhibit a platy morphology, indicating that the morphology of SFCA (and also SFCA-I) is the result of a complex interaction between maximum temperature, holding time, and cooling rate. For example, short holding times at maximum temperature will generate a large amount of smaller crystals, with the morphology of the SFCA coarsening if left for longer holding times as crystals growth occurs.

Electron Probe Microanalysis

Two of the compact samples were examined by EPMA; samples 1 and 10. Sample 1 was produced at a low temperature (1250°C), where SFCA-I may be stable.[5] In comparison, sample 10 was produced at 1320°C, likely to be beyond the stability range for SFCA-I. Optical microscopy of sample 1 identified regions of platy SFCA (~ 18.8% by area) columnar SFCA and regions comprising a phase classified as "dense SFCA". The higher-temperature sample had little or no platy SFCA. The two samples were examined using EPMA mapping, and quantitative analyses on the different morphological types were

Table III. Comparison between point counting and bulk XRD results (mass%)

	Reflected light microscopy					Bulk XRD			
Sample #	Hematite[a]	Magnetite	Platy SFCA	Columnar SFCA	C2S	Hematite	Magnetite	SFCA	C2S
1	58.8	5.5	14.9	15.8	1.6	47.3	4.2	45.7	2.8
2	51.9	2.0	17.6	25.0	1.3	43.3	10.1	41.9	4.2
4	53.4	1.7	3.4	39.4	0.0	47.1	3.4	47.7	1.7
7	53.6	4.3	4.4	34.1	1.5	35.0	4.8	57.0	2.8
10	45.7	20.2	1.7	25.3	4.3	44.5	19.8	32.1	3.6
11	46.1	13.7	1.1	36.2	1.2	30.6	19.4	47.0	2.5
12	16.0	52.9	0.3	22.2	3.7	13.0	57.3	26.7	3.0
13	33.2	35.6	0.0	27.7	1.5	4.5	49.0	44.9	1.7

[a]Reflected light microscopy enables identification of primary and secondary hematite; however, in this table, both morphological types have been combined to enable direct comparison with the bulk XRD data.
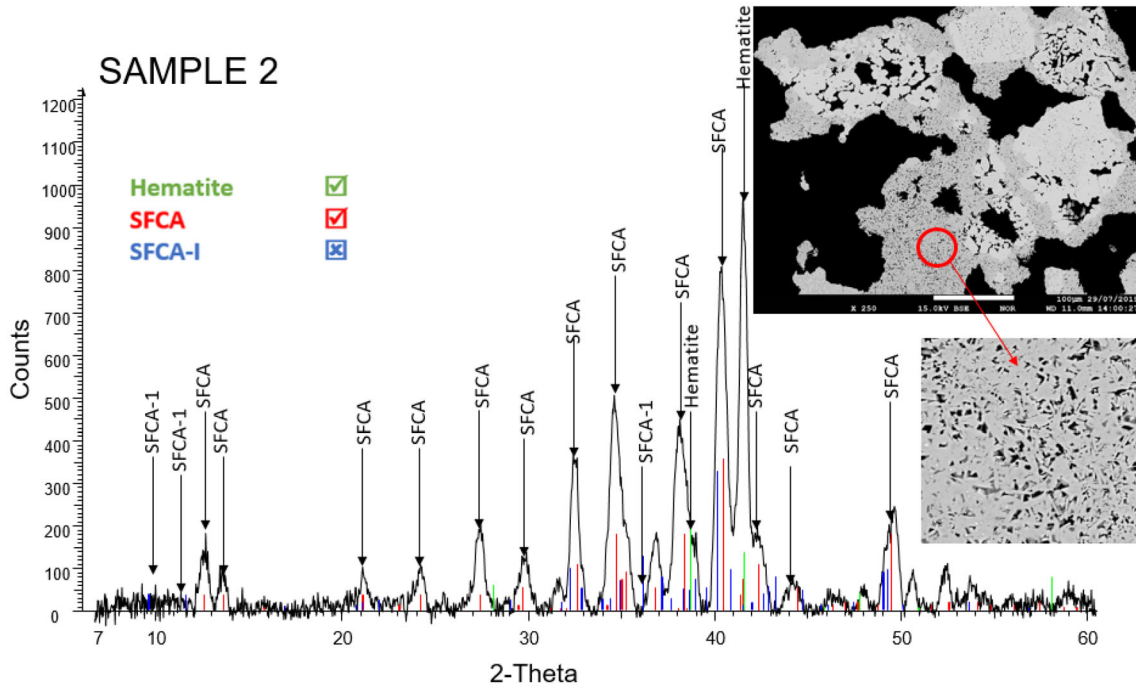
Fig. 3. Micro-XRD analysis of sample 2. back-scattered electron images highlighting the platy morphology of the area selected for analysis.

obtained. Compositional differences exist between SFCA and SFCA-I[15] and regions containing these phases (i.e., areas of columnar and platy SFCA morphology, respectively) were examined in detail. In addition, a region in sample 1 of "dense SFCA' was examined to determine if this phase varied in composition from typical SFCA or SFCA-I.

Sample 1: (T = 1250°C, 1 min holding time, 5°C/s cooling rate)

Two areas were mapped (Fig. 4). Area 1 covered a region identified optically as "dense SFCA" (particle in center of Fig. 4a) with some coarse columnar SFCA present. Area 2 was a region which exhibited a fine, platy morphology thought to be characteristic

of SFCA-I. In Area 1, the phase assemblage comprised magnetite, hematite, two 'SFCA types', and a dense Ca–Mg-containing ferrite phase. For Area 2, the same two types of SFCA phase as observed in Area 1 were present; however, there was no dense ferrite. Quantitative EPMA data for individual phases within Areas 1 and 2 indicated the following:

- Hematite was low in total impurities.
- Magnetite was distinguished from hematite by a higher level of impurities with an average composition: $\sim 87\%$ FeO; $\sim 2\%$ CaO; $\sim 1\%$ Al_2O_3, and $\sim 4\%$ MgO
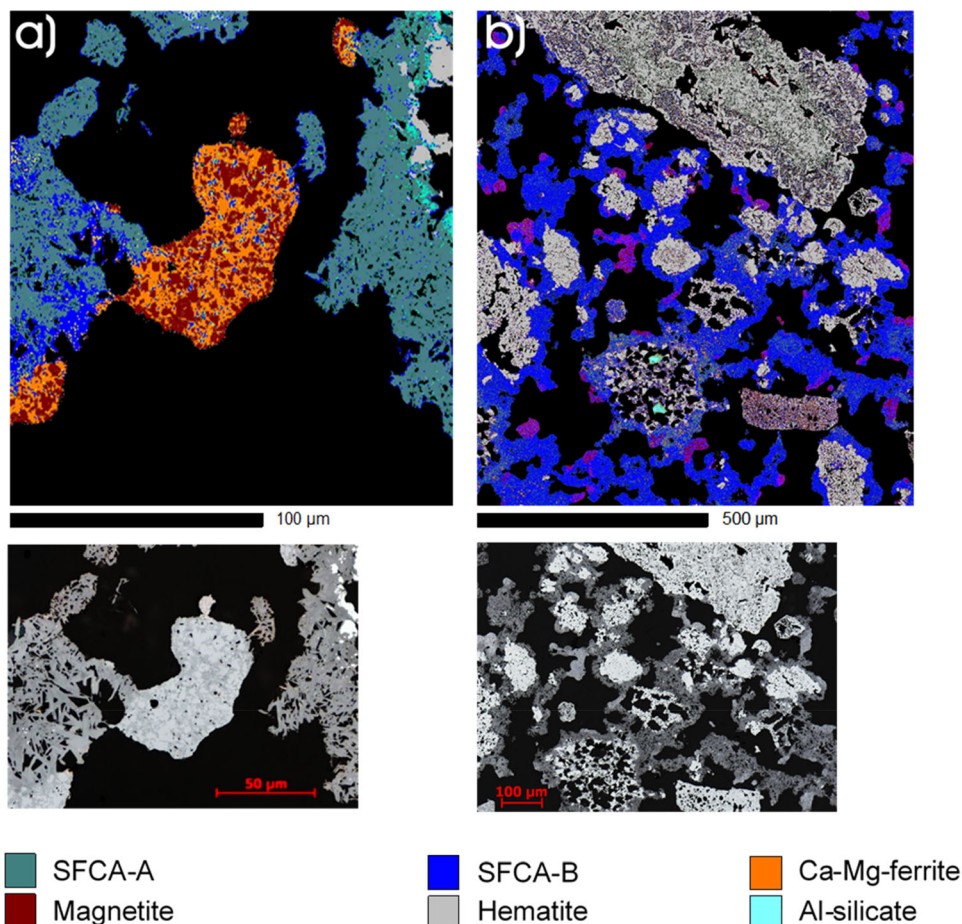- The phase labeled SFCA-A had the average

Fig. 4. Reflected light photomicrographs and corresponding EPMA maps showing the distribution of phases within sample 1 (T = 1250°C, 1 min holding time, 5°C/s cooling rate), (a) area 1, (b) area 2. Note the difference in scale between the two areas imaged.

composition: 70–72% FeO; 5–6% SiO$_2$; 14–15% CaO; 3.5–4.0% Al$_2$O$_3$ and < 1% MgO.

- The SFCA phase in close association with magnetite (SFCA-B high-Mg) was high in iron and magnesium, with average composition: $\sim$ 75% FeO; 2.5–3.0% SiO$_2$; $\sim$ 12% CaO; 2.0–2.5% Al$_2$O$_3$, and 2.0–2.5% MgO.
- The phase thought to represent "dense SFCA", has a composition of 82% FeO; 4.5% CaO; 6.5% MgO, and 2% of both Al$_2$O$_3$ and SiO$_2$. This phase appears to be a Ca–Mg ferrite.

Based on the compositions listed above, no SFCA-I was identified, in contrast to the point counting results but in agreement with the QXRD results.

Sample 10 was selected for analysis as the only variation from sample 1 was that the holding temperature was 70°C higher—all other experimental parameters remained constant. Point counting suggests a phase with platy SFCA-I-like morphology is present whereas measurements indicate only SFCA phase.

Results in Fig. 5 show two different SFCA types are present: SFCA-A phase with the averaged composition: 69% FeO; 6% SiO$_2$; 14% CaO; 6%

Al$_2$O$_3$, and < 1% MgO, and a second high-Mg SFCA type (SFCA-B) that occurs adjacent to magnetite with the averaged composition: 74% FeO; 4% SiO$_2$; 11% CaO; 5% Al$_2$O$_3$, and $\sim$ 1.6% MgO. Both SFCA types are essentially the same as the SFCA-A and SFCA-B (high-Mg) phases observed in sample 1 but with slight differences in compositions (in particular Al$_2$O$_3$) due to different amounts of substitutional components entering the structure. The primary conclusion from examination of sample 10 is that, although parts of the sample contain a morphology that is usually recognized as being characteristic of SFCA-I, no SFCA-I is present, consistent with the QXRD results. Other phases present included magnetite and quench glass.

The EPMA data indicate that the major phases present in the samples included: SFCA (two types, hematite, glass) and a Ca–Mg ferrite-like phase which is associated with magnetite. The latter phase is typically present as a dense, low-porosity structure which may previously have been incorrectly characterized as "dense SFCA". There was no evidence of any SFCA-I within any of the areas mapped, consistent with the QXRD results which
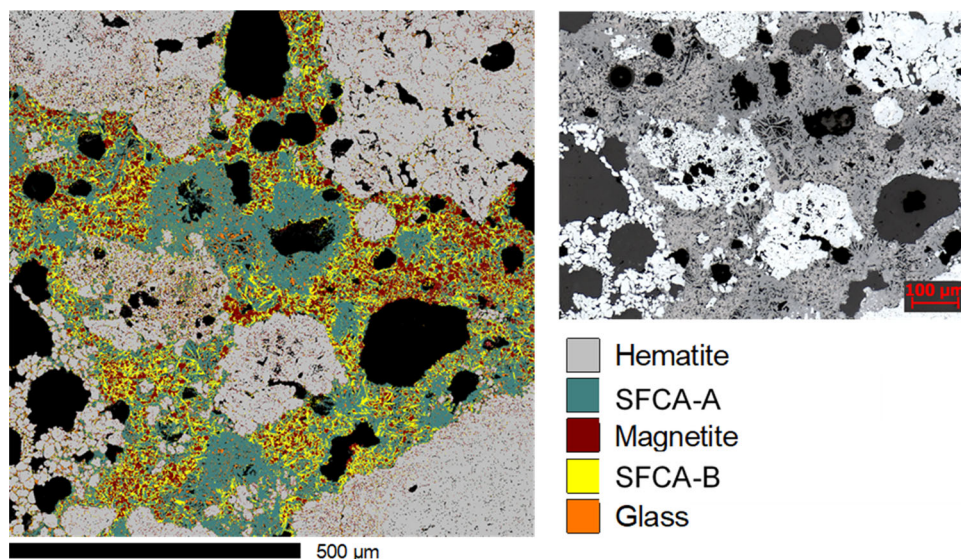
Fig. 5. Reflected light photomicrographs and corresponding phase patched EPMA map showing the distribution of phases within sample 10 (T = 1320°C, 1 min holding time, 5°C/s cooling rate).

indicated that none of the samples contained SFCA-I.

The quantitative analyses obtained for the SFCA phase(s) in each sample are typical of the range of compositions previously indicated for the SFCA solid-solution series.[15] Differences between samples presumably reflect different proximity to source components e.g., if SFCA forms close to an aluminous gangue particle, it will necessarily contain a greater amount of Al. Similarly, if the SFCA is near or surrounded by magnetite, it will typically be higher in MgO.

An important conclusion from the EPMA data is that texture is not a reliable indicator of SFCA phase type. Although point counting indicated that the fine platy morphology characteristic of SFCA-I was present in two of the samples (1 and 10), the quantitative EPMA results demonstrated that this morphology was in fact SFCA phase. This is consistent with previous studies on the stability of SFCA-I and SFCA[5] which show that, at the temperatures the compact experiments were run, SFCA-I should not be stable. Our inference is that the morphologies observed in these samples are due to factors such as the peak temperature and, importantly, holding time at the peak temperature. It is reasonable to assume that rapid heating combined with low holding time at peak temperature results in smaller, acicular crystals (i.e., platy) that can be mistaken for SFCA-I. Likewise, holding the sinter mixture at high temperature for a longer time results in the growth of larger crystals. This is not to say that SFCA-I does not exist in sinter, which it clearly does, but that classifying the amount present of SFCA-I versus SFCA in a sinter mixture using morphology as the discriminating feature may

lead to erroneous results. Importantly for future studies, researchers should be careful to clearly specify whether their analysis technique is based on point counting or XRD; XRD studies can rightly claim to identify the minerals SFCA and SFCA-I, whereas reflected light microscopy can correctly identify a range of SFCA morphologies such as the platy and columnar SFCA described here. The identification and presence of different morphological features will likely have implications for reducibility.

Reducibility

Typical reduction curves for a range of analogue sinter samples are given in Fig. 6a. The reducibility of the sinter analogue tablets increased compared to unfired analogues when fired to a maximum temperature of 1250°C or 1285°C. Bristow and Waters[32] found a similar trend for analogue sinters fired at 1300°C and reduced at 900°C, although the trend was the opposite for low temperature reduction at 550°C. When the maximum temperature was increased to 1320°C, the reducibility decreased to below that of the unfired analogue. The morphology of samples produced at this temperature contained higher proportions of magnetite and glass components, which was confirmed by the bulk XRD data for these samples. It is well known that a trade-off exists between sinter strength and reducibility, with very high fuel rates leading to stronger but less reducible sinter.[33] Oyama[34] determined that the sinter reducibility and strength could be optimized by increasing the time spent at sintering temperatures above 1200°C, while limiting the maximum temperature to < 1400°C in sinter pot
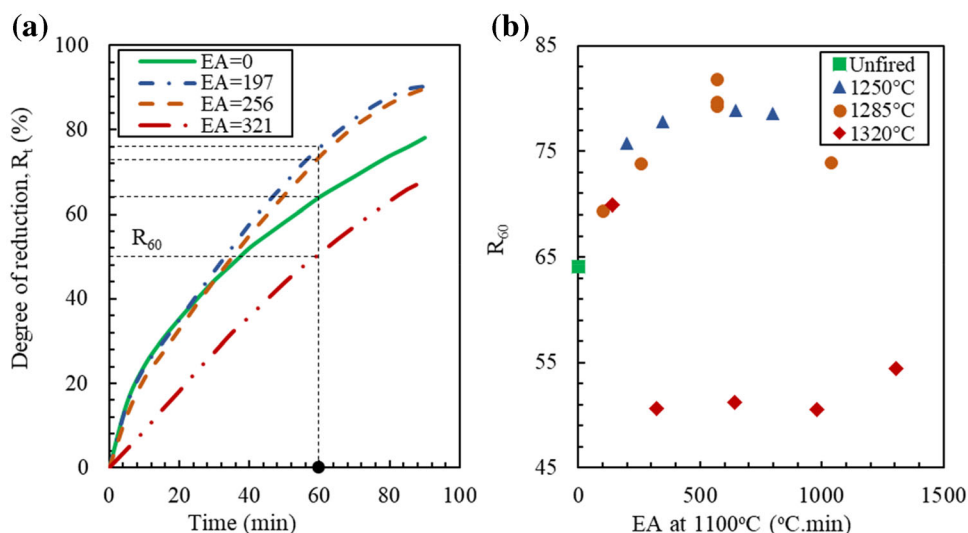
Fig. 6. (a) Reduction curves for a range of analogue sinter tablets at 900°C, 30% CO in N_2, (b) degree of reduction after 60 min (R60) versus EA.

Table IV. Analogue sinter tablet degree of reduction at 60 min (R60)

Sample #	Maximum temperature (°C)	Holding time (min)	Cooling rate (°C/s)	R60 (%)
1	1250	1	5	75.8
2	1250	1	1	77.8
3	1250	4	5	78.9
4	1250	4	1	78.6
5	1285	0.17	5	63.9
6	1285	1	5	73.8
7	1285	2.5	3	80.2
8	1285	4	1	73.9
9	1320	0.17	5	70.0
10	1320	1	5	50.6
11	1320	1	1	51.2
12	1320	4	5	50.5
13	1320	4	1	54.4

and plant trials through the injection of secondary fuel. In practice, the maximum temperatures measured using thermography in the pot tests were 1300°C when using secondary fuel injection, leading to an improvement in reducibility of 6% over all coke sinter tests with a maximum temperature of up to 1500°C. Some differences are expected in the behavior of analogue sinters heated using infra-red energy and pilot-scale sinters heated using coke combustion; however, the trend of a decrease in reducibility above a critical maximum temperature is similar.

The degree of reduction after 60 min (R60) was taken as a measurement of the analogue sinter reducibility, and these values are given in Table IV. The R60 results are plotted against EA in Fig. 6b, showing that the R60 generally increases with increasing EA for maximum sintering temperatures of 1250°C and 1285°C up to a point ($\approx$ 800 C/min), above which there is a decrease. Similar results

were found by Harvey et al. (2020)[18] for sinter strength. For the sintering temperature of 1320°C, the R60 is consistently low, regardless of EA.

The R60 results are plotted against the morphology of the sinter determined by point counting and the mineralogy determined by XRD in Fig. 7. It is apparent from Fig. 7a and b that little correlation exists between the R60 and morphology for these analogue sinter tablets. The expected relationship between platy SFCA and reducibility is not apparent. There is a clear effect of maximum temperature during sintering, as shown in Fig. 6b, with all but the very short hold time samples with a maximum temperature of 1320°C having a significantly lower reducibility. There is some indication from Fig. 7c that the reducibility of R60 is lower in samples where more than 10% magnetite is present, determined by either point counting or XRD.

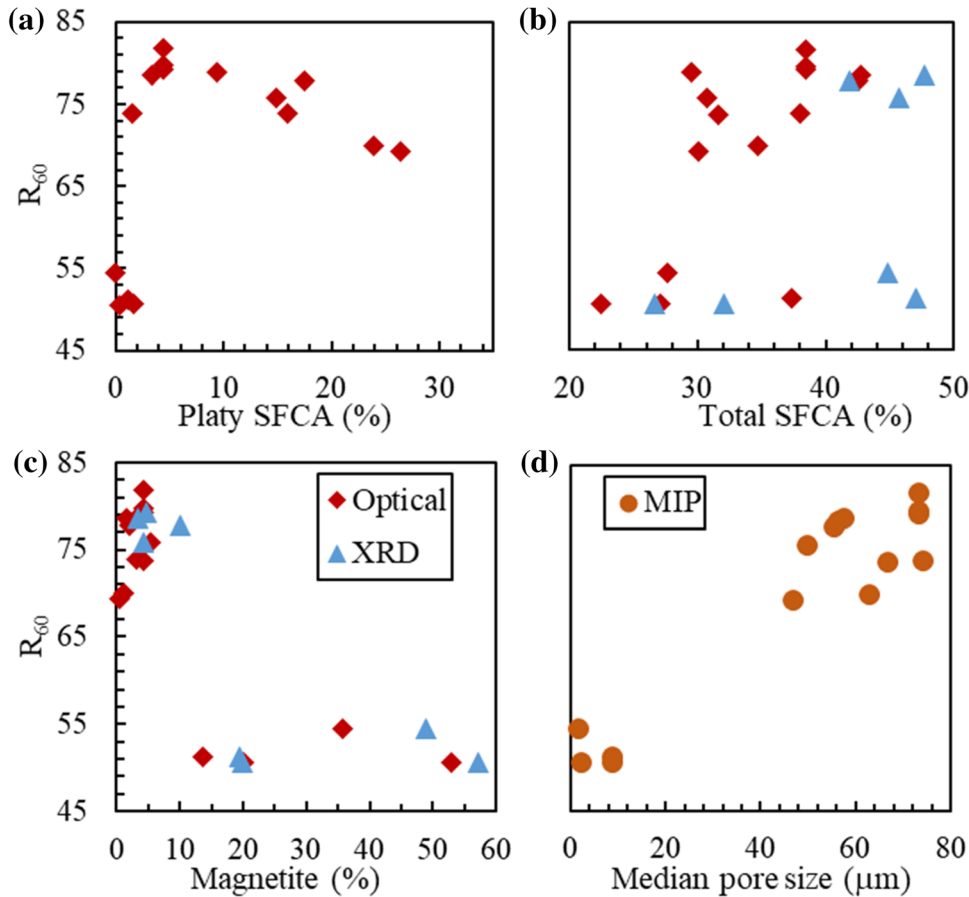Figure 7d plots the reducibility (R60) against the median pore diameter of the sinter analogue tablets.

Fig. 7. Degree of reduction measured after 60 min (R60) versus (a) platy SFCA morphology by reflected light microscopy, (b) total of all SFCA morphologies by reflected light microscopy and XRD, (c) magnetite by reflected light microscopy and XRD, and (d) median pore size by mercury intrusion porosimetry (*MIP*).

These results suggest that the macro-porosity of the sinter analogue tablets has a strong influence on the reducibility, with access of reducing gas to the interior of the tablets dominating over the increased surface area for reaction of finer pores, or the intrinsic reducibility of the phases present. Bristow and Waters[32] performed a more comprehensive study of the effect of porosity on the reducibility of sinter in comparison to the original iron ore, finding that sinter retained its fine pore structure (pores with diameter < 1 μm) during reduction, and that these pores increased as reduction proceeded, whereas pores of this size in the parent ore decreased.

Further work is required to examine the interaction between the physical structure of the sinter, in particular the porosity, and the mineralogy and morphology of the SFCA phases, as the two are clearly linked.

CONCLUSION

Analogue sinter tablets were produced under a range of maximum temperatures, holding times, and cooling rates, giving a wide range of enclosed area values.

The platy and columnar SFCA morphologies determined by reflected light microscopy were both shown to have SFCA mineralogy by bulk and micro-XRD analysis. It is not valid to assume that platy SFCA by reflected light microscopy is equivalent to SFCA-I.

The morphology of SFCA in the sinter analogues was found to be a function of the maximum temperature and time at temperature, with longer times and higher temperatures leading to coarsening of the crystal structure.

The reducibility of sinter analogues was found to vary with maximum sintering temperature, with the highest reducibility obtained at sintering temperatures of 1250–1285°C. The morphology of mineral phases in the analogue sinters showed poor correlation with reducibility. In this study, reducibility was controlled by the porosity of the tablets, rather than by the mineral content.

ACKNOWLEDGEMENTS

and permission to publish this paper. The University of Wollongong is acknowledged for access to the tube furnace TGA.

CONFLICT OF INTEREST

On behalf of all authors, the corresponding author states that there is no conflict of interest.

OPEN ACCESS

REFERENCES

1. J. Hancart, V. Leroy and A. Bragard, *CNRM Metall. Rep.,* 3 (1967).
2. J.G. Hamilton, B. Hoskins, W. Mumme, W. Borbidge, and M. Montague, *Neues Jahrb. Mineral. Abh.* 161, 1 (1989).
3. M. Sasaki and Y. Hida, *Tetsu-to-Hagané* 68, 563 (1982).
4. N.V.Y. Scarlett, M.I. Pownceby, I.C. Madsen, and A.N. Christensen, *Metall. Mater. Trans. B* 35, 929 (2004).
5. N.A. Webster, M.I. Pownceby, I.C. Madsen, and J.A. Kimpton, *Metall. Mater. Trans. B* 43, 1344 (2012).
6. Y. Hida, J. Okazaki, K. Itoh, and M. Sasaki, *Tetsu-to-Hagané* 73, 1893 (1987).
7. R. Mežibrický and M. Fröhlichová, *ISIJ Int.* 56, 1111 (2016).
8. T. Takayama, K. Higuchi and J. Okazaki, Study on multi-component calcium ferrites formation by using XRD-Rietveld analysis, *Iron Ore Proceedings*, (2019), pp. 166.
9. B. Cai, T. Watanabe, C. Kamijo, M. Susa, and M. Hayashi, *ISIJ Int.* 58, 642 (2018).
10. D. Maruoka, S. Mataoka, T. Murakami and E. Kasai, Influence of crystal structure and chemical composition of silico-ferrite of calcium and aluminum on its reducibility, *ICSTI International Conference Proc.*, Vienna, Austria, (2018), pp. 25.
11. W. Mumme, J. Clout and R. Gable, *Neues Jahrb. Mineral. Abh.,* 93 (1998).
12. S. Ahsan, T. Mukherjee, and J. Whiteman, *Ironmaking Steelmaking* 10, 54 (1983).
13. W. Mumme, *Neues Jahrb. Mineral. Abh. J. Mineral. Geochem.* 178, 307 (2003).
14. Y. Ishikawa, Y. Shimomura, M. Sasaki, Y. Hida and H. Toda, Improvement of sinter quality based on the mineralogical properties of ores, *Ironmaking Proceedings*, (1983), pp. 17.
15. S. Nicol, J. Chen, M.I. Pownceby, and N.A. Webster, *ISIJ Int.* 58, 2157 (2018).
16. T. Honeyands, J. Manuel, L. Matthews, D. O'Dea, D. Pinson, J. Leedham, G. Zhang, H. Li, B. Monaghan, and X. Liu, *Minerals* 9, 333 (2019).
17. T. Murakami, T. Kodaira, and E. Kasai, *ISIJ Int.* 55, 1197 (2015).
18. T. Harvey, T. Honeyands, D. O'dea, and G. Evans, *ISIJ Int.* 60, 73 (2020).
19. C.E. Loo, N. Tame, and G.C. Penny, *ISIJ Int.* 52, 967 (2012).
20. L.-H. Hsieh and J.A. Whiteman, *ISIJ Int.* 29, 24 (1989).
21. Malvern Panalytical. X'Pert HighScore Plus; Version 4; PANalytical B V, Almelo, The Netherlands, 2014., (2014).
22. H. Rietveld, *J. Appl. Crystallogr.* 2, 65 (1969).
23. Bruker AXS, TOPAS V5. General Profile and Structure Analysis Software for Powder Diffraction Data; Bruker AXS, Karlsruhe, Germany, 2013.
24. I. Harrowfield, C. MacRae and N. Wilson, (1993).
25. N. Wilson and C. MacRae, *Microsc. Microanal.* 11, 434 (2005).
26. J. Pouchou, *Microbiol. Anal.* 20, 104 (1985).
27. J.-L. Pouchou and F. Pichoir, *Quantitative analysis of homogeneous or stratified microvolumes applying the model "PAP", Electron probe quantitation* (Berlin: Springer, 1991), p. 31.
28. DiffracPlus Eva software version 10.0, Year 2004, by Bruker AXS, Karlsruhe, Germany, (2004).
29. ICDD (2004). PDF-2. International Centre for Diffraction Data, Newtown Square, PA, USA.
30. ISO7215, 2015, Iron ores for blast furnace feedstocks — Determination of the reducibility by the final degree of reduction index. International Organization for Standardization, Geneva Switzerland., (2015).
31. C. Loo, R. Williams, and L. Matthews, *Trans. Inst. Min. Metall., Sect. C* 101, C7 (1992).
32. N. Bristow and A. Waters, *Trans. Inst. Min. Metall. C Miner.,* 100, (1991).
33. P. Dawson, J. Ostwald and K. Hayes, The influence of the sintering temperature profile on the mineralogy and properties of iron ore sinters, *AIMM Bull. Proc.*, (1984), pp. 163.
34. N. Oyama, Y. Iwami, T. Yamamoto, S. Machida, T. Higuchi, H. Sato, M. Sato, K. Takeda, Y. Watanabe, and M. Shimizu, *ISIJ Int.* 51, 913 (2011).